



Cite this: *J. Mater. Chem. C*, 2022, **10**, 17925

Identification of distinctive structural and optoelectronic properties of Bi_2O_3 polymorphs controlled by tantalum addition[†]

Taro Saito,^{‡,a} Rafia Ahmad,^{‡,b} Fuminao Kishimoto,^{ID, a} Tomohiro Higashi,^{ID, c} Masao Katayama,^d Luigi Cavallo^{ID, *b} and Kazuhiro Takanabe^{ID, *a}

Diverse crystal phases of bismuth (Bi) oxides induced by the addition of different amounts of tantalum (Ta) were synthesized. Their optoelectronic and redox properties were quantitatively investigated using combined experimental and computational approaches. Synthesis conditions that transform α - Bi_2O_3 into β - Bi_2O_3 and δ - Bi_2O_3 in terms of the Ta quantity, as well as synthesis temperatures, are identified and demonstrated. The phase transition behavior and crystal structures were characterized by *in situ* high temperature X-ray diffraction (XRD), thermogravimetry–differential thermal analysis (TG/DTA), X-ray absorption near edge structures (XANES), and extended X-ray absorption fine structures (EXAFS). Density functional theory calculations employing the HSE exchange–correlation functional with spin–orbit coupling were used to quantitatively simulate the optoelectronic properties and band structures of β - Bi_2O_3 and δ - Bi_2O_3 . Along with the absorption coefficient and density of states, effective masses and dielectric constants were elucidated. The characterization study confirmed the distortion of Ta–O bonds in the Ta-supplemented β - Bi_2O_3 and the substitutional positions of the Bi and Ta atoms in the δ - Bi_2O_3 and Bi_3TaO_7 compounds. The reducibility of these oxides was strongly influenced by the crystal phase confirmed by temperature-programmed reduction (TPR) analysis. These findings can be used as a bismuth oxides' benchmark for optoelectronic applications as well as thermal catalysis as the redox active center or the support.

Received 3rd September 2022,
Accepted 5th November 2022

DOI: 10.1039/d2tc03718a

rsc.li/materials-c

Introduction

Bi_2O_3 is one of the polymorphous oxides, and is employed in a broad range of applications such as solid-state electrocatalysis,^{1–6} inorganic orange pigment,⁷ and photocatalytic reactions.^{8–27} To date, four different crystal phases have been reported: α phase (monoclinic), β phase (tetragonal), γ phase (cubic), and δ phase (cubic). Among the polymorphs, the α phase is the most stable phase at room temperature. The high-temperature-stable δ phase is transformed into the β or γ phase while cooling, which results

in the further transformation into the α phase at room temperature.²⁸ While the δ phase shows a high O^{2-} ion conductivity, applicable to mid-temperature electrocatalysis at 300–500 °C,^{1–5} β - Bi_2O_3 attracts attention as a photocatalyst due to a narrow bandgap of ~ 2.2 eV.^{8–12}

Solid-state synthesis of pure Bi_2O_3 has been well reported in the literature.²⁸ Knowing the melting point of Bi_2O_3 to be ~ 830 °C, phase transition temperatures have been studied in detail. Nevertheless, selective synthesis of specific phases from pure Bi_2O_3 remains challenging. By doping α - Bi_2O_3 with a trace amount of oxides, such as Ta_2O_5 , CeO_2 , ZrO_2 , EuO_x , TiO_x , and MnO_x ,^{5,7,29–33} a solid-state reaction at a high temperature becomes possible to make metastable β -, γ -, and δ -phases recoverable for successive applications. Recently, Masui and coworkers reported the addition of Ta_2O_5 into α - Bi_2O_3 to synthesize β - and δ -phases, and among them, β - Bi_2O_3 was recognized to have a potential to be an orange pigment with its vivid orange color due to its unique bandgap narrowing.⁷ This bandgap with a visible light response may be suitable for solar energy conversion, but the investigation of β - Bi_2O_3 as a photocatalyst, especially for application in photosynthetic reactions, has been limited.⁹ The details of how Ta induces the

^a Department of Chemical System Engineering, School of Engineering, The University of Tokyo, 7-3-1, Hongo, Bunkyo-ku, Tokyo 113-8656, Japan.

E-mail: takanabe@chemsys.t.u-tokyo.ac.jp

^b King Abdullah University of Science and Technology (KAUST), KAUST Catalysis Center (KCC), 4700 KAUST, Thuwal 23955-6900, Saudi Arabia

^c Institute for Tenure Track Promotion, University of Miyazaki, Nishi 1-1 Gakuen-Kibanadai, Miyazaki 889-2192, Japan

^d Environmental Science Center, Department of Chemical System Engineering, The University of Tokyo, 7-3-1, Hongo, Bunkyo-ku, Tokyo 113-8656, Japan

† Electronic supplementary information (ESI) available. See DOI: <https://doi.org/10.1039/d2tc03718a>

‡ These authors contributed equally.



crystal phase transition and narrows the bandgap also remain unclarified.

The purpose of this study is to provide not only explicit synthesis protocols for each crystal structure, but also quantitatively analyse various optoelectronic and redox properties of bismuth oxides. Different Bi_2O_3 phases and Bi_3TaO_7 were successfully achieved by varying the Ta/Bi ratio (0.020–0.333). The obtained materials were characterized by *in situ* X-ray diffraction (XRD), X-ray absorption spectroscopy (XAS), diffuse-reflectance ultraviolet-visible spectroscopy (DR-UV-vis), and photoelectron spectroscopy in air (PESA). The optoelectronic structure was studied both experimentally and theoretically to understand their density of states (DOS), dielectric properties, and effective masses. Photoelectrochemical (PEC) measurements and temperature-programmed reduction (TPR) analyses were conducted.

Experimental and theoretical

Synthesis

Ta_2O_5 (99.9%, Kojundo Chemical Laboratory Co., Ltd.) was mixed with Bi_2O_3 (98.0+%, FUJIFILM Wako Pure Chemical Corporation) ($0.020 \leq \text{Ta/Bi} \leq 0.333$) using a mortar and pestle. Heat treatment was usually conducted at 850 °C, with a heating rate of 10 °C min⁻¹ and was held at this temperature for 5 h in a muffle furnace in air. During the heat treatment, the mixtures were placed on an Alumina boat (Nikkato, SSA-S grade, Al_2O_3 99.6%) to prevent contamination of silica components. Then, the samples were cooled naturally in the furnace by turning off the electric power. The samples were ground in an Alumina boat prior to characterization.

X-ray diffraction

The powder XRD patterns were collected using a Rigaku Ultima III equipped with a copper (Cu) X-ray source operated at 40 kV and 40 mA. The diffractometer was configured with a 1/2° divergence slit limited to 10 mm, an open scattering slit, an open receiving slit, and a nickel (Ni) filter to attenuate contributions from Cu-K β fluorescence. The data sets were acquired in continuous scanning mode (20° min⁻¹) with an integration step size of 0.02°; however, when focusing on certain peaks (*i.e.*, only around $2\theta = 26\text{--}29^\circ$), these parameters were set to 1° min⁻¹ and 0.01°, respectively. The peak positions were calibrated using the secondary peak of silicon (Si) (standard, 220, 47.2660°, cubic, Fd3m). *In situ* high-temperature XRD was performed using an attachment (Reactor-X, Rigaku) equipped with an infrared heater connected to its controller (PTC EVO, Rigaku) and an external power source (Thermo plus EVO PU-4K CE, Rigaku). An infrared reflector was attached to assist in heating the sample, while the attachments were continuously cooled with circulating water and both an external and internal fan. With this setup, the peak positions were calibrated using the secondary peak of Si powder (Wako, 220, 47.2660°, cubic, Fd3m) at room temperature. The temperature was increased with a heating rate of 10 °C min⁻¹ from room

temperature to 830 °C and 2 °C min⁻¹ from 830 °C to 850 °C to prevent the cell from overheating. The temperature was decreased with a cooling rate of 10 °C min⁻¹ to 25 °C, and the determined temperature was held for 5 min before each measurement. All measurements were conducted by flowing a mixture of 80 mL min⁻¹ argon (Ar) and 20 mL min⁻¹ O₂. The temperature was corrected by using the α to δ phase transition peak (in the heating process) of Bi_2O_3 (98.0+%, Wako Pure Chemical Corporation) at 735 °C.

X-ray absorption spectroscopy

Bi L₃-edge and Ta L₃-edge XAS were performed at the bending magnet XAFS beamline, BL01B1 at SPring-8 (Hyogo, Japan). Experiments were performed at room temperature and in the transmission mode using the ionization chambers. Bi_2O_3 and Ta_2O_5 were used as references. The powder samples were thoroughly ground with boron nitride in an agate mortar, and 10 mm-diameter pellets were made. The amount of boron nitride was ~90 mg to ensure that the pellets could be handled without breaking. The EXAFS spectra were analyzed using the HORAE-IFEFFIT (Athena) program package. This program enabled us to normalize the absorption coefficient, $\mu(k)$, and to separate the oscillatory EXAFS, $\chi(k)$, from the absorption background. Before normalization, the pre-edge range of the spectra for Bi and Ta L₃ edges was flattened in the energy range of -210 to -60 keV and -200 to -60 keV, respectively. The data sets for Bi and Ta L₃ edges were normalized in the energy range of 50–880 keV (4.0–71.0 Å⁻¹) and 200–1000 eV (16.1–80.7 Å⁻¹), respectively. Then, the background was calculated from the data in energy ranges of 0–15 Å⁻¹ (0–857 eV) for Bi L₃ edges and 0–17 Å⁻¹ (0–1001 eV) for Ta L₃ edges. All data were Fourier-transformed using the same k range, $k = 3\text{--}12 \text{ \AA}^{-1}$, k weighting of 2 and a hanning k window and plotted with k weighting of 3. The theoretical radial distribution functions were calculated using the Visual Molecular Dynamics (VMD) program (version 1.9.4a49).³⁴

Band position determination

DR-UV-vis and PESA were performed to determine the band alignment of the conduction band minimum (CBM) and the valence band maximum (VBM) positions of the synthesized samples. DR-UV-vis spectroscopy was performed on a JASCO model V-770 spectrophotometer equipped with an integrating sphere. The reflectance spectra were scanned over the range of 200–1000 nm with a scan speed of 400 nm min⁻¹ and a bandwidth of 2.0 nm for the ultraviolet/visible region and 8.0 nm for the near-infrared region. The reflectance spectra were referred to the background reflectance of BaSO₄ powder. The contributions of scattering were removed by the Kubelka-Munk function, $F(R_\infty)$. Followed by the calculation of the bandgap energy, the absorption edge was determined by the intercept of the straight line extrapolated to the $F(R_\infty)$ vs wavelength.

The valence band positions were determined by PESA (AC-3 photoelectron spectrometer, Riken Keiki Co., Ltd.). The obtained spectra were calibrated based on the work function of gold (Au) (5.30 eV *vs.* vacuum).³⁵ The yield of the photoelectrons was



measured for 30 s at every 0.1 eV step in the range of 4.0–7.0 eV of irradiation UV light. The valence band potentials, obtained as the potentials relative to the absolute vacuum potential, were converted to the standard hydrogen potentials ($E_{\text{SHE}} = E_{\text{abs}} - 4.44$ V). The conduction band positions were calculated from the valence band positions, and the bandgaps were determined by PESA and DR-UV-vis spectroscopy.

Photoluminescence

Photoluminescence (PL) spectroscopy was performed on a JASCO model FP-8500 fluorescence spectrometer operated at liquid nitrogen temperature under ambient pressure. The excitation and emission had a 5 nm bandwidth. The spectra were scanned at a speed of 1000 nm min⁻¹ with medium level sensitivity and 50 ms of response at every 0.1 nm interval and accumulated over 10 cycles.

Thermogravimetry/differential thermal analysis

TG/DTA was performed to investigate the phase transition processes of Ta_2O_5 -supplemented Bi_2O_3 *in situ*. TG/DTA was performed using a Thermo plus EVO2 series TG-DTA 8120 (Rigaku) in the atmosphere of the residual air in the chamber without flow. All measurements were performed with a 10 °C min⁻¹ heating rate and cooling rates of up to 850 °C. The sample (8–10 mg of the Bi_2O_3 powder or the mixture of Bi_2O_3 and Ta_2O_5 powders mixed at the stoichiometric amounts [Ta/Bi = 0.05, 0.10]) was placed in an open platinum pan. An open and empty platinum pan was used as the reference.

Scanning electron microscopy (SEM) and elemental analysis

The morphologies, particle sizes, and the layered structure of the particulate photoelectrodes were examined using a high-resolution field emission SEM (FE-SEM; JEOL, JSM-IT800) equipped with a secondary electron detector. Energy-dispersive X-ray spectroscopy (EDS) was conducted with an EDS detector (Ultim Max, Oxford Instruments).

Computational method

All calculations were performed using the Vienna *Ab initio* Simulation Package (VASP),^{36,37} with the projector augment wave (PAW) method.³⁸ Calculations were performed with the cut-off energy set to 400 eV. Brillouin zone sampling was performed using Monkhorst and Pack schemes.³⁹ We completely relaxed the bulk unit cell of $\beta\text{-Bi}_2\text{O}_3$ in its tetragonal structure with space group $P\bar{4}21c$, which contains 8 Bi atoms and 12 oxygen (O) atoms. $\delta\text{-Bi}_2\text{O}_3$ has a cubic fluorite structure with a space group of $Fm\bar{3}m$. The unit cell contains two Bi_2O_3 formulas. The valence atomic configurations are 5d¹⁰ 6s² 6p³ for Bi and 2s² 2p⁴ for O atoms. Geometry optimizations were terminated when the energy and force on each ion were reduced below 10⁻⁶ eV and 0.02 eV Å⁻¹, and the optimized structures were then used to calculate the electronic structures. Hybrid DFT calculations were performed at a single point at the generalized gradient approximation (GGA) lattice geometry.⁴⁰ First, the GGA scheme was employed for the fully-relaxed structural optimization. Then, the screened-exchange hybrid

functional of Heyd, Scuseria, and Ernzerhof (HSE06),^{41,42} representing the electronic exchange–correlation energy, was adopted for calculations of the electronic and optical properties. The spin–orbit coupling (SOC) effect was taken into consideration through the second variational method because of the relativistic effect in Bi atoms.⁴³ More details of the computational modeling of surfaces and of the methodology used to calculate the optical properties can be found in the ESI.†

Electrochemical (EC) and photoelectrochemical (PEC) measurements

To conduct EC and PEC measurements, particulate photoelectrodes were fabricated through previously reported particle transfer methods.⁴⁴ Multilayers of photocatalyst particles were deposited on a glass plate by drop-casting and drying its suspension in isopropanol several times, resulting in an approximate amount of 10 mg cm⁻². Subsequently, 200 nm-thick-Ti and 3–4 μm-thick-Sn were sequentially deposited on the particles through electron beam deposition (ULVAC) to prepare the assembly of photocatalysts with a Ti–Sn conductive layer. The obtained assembly of particles and the Ti–Sn layer adhering to them were peeled off from the glass plate, and the excess unused particles piled up on the deposited particles were removed by ultrasonication in ethanol. The film electrode was fixed on another glass plate using carbon tape. Finally, the film was connected to lead wire using an indium solder, after which its unnecessary part was covered with epoxy resin for insulation. The geometrical electrode areas of the photoelectrodes were approximately 0.20–0.30 cm². EC and PEC measurements for the particulate-photoelectrodes were performed using a three-electrode system under an argon (Ar) gas atmosphere at a temperature of 25 °C. The Hg/Hg₂Cl₂/saturated KCl reference electrode (BAS Inc., RE-2BP, 241 mV vs. RHE at 25 °C) and coiled-Pt wire counter electrode were connected to a potentiostat (SP-150, BioLogic Science Instruments). Prior to the PEC measurements, a CoO_x catalyst promoting the carrier transfer at the solid–liquid interface was electrodeposited under light irradiation on the surface of the particulate photoelectrodes. A solar simulator (XES-40S2, SAN-EI Electric Co., Ltd.) equipped with an AM 1.5G filter was used as the light source, and the light intensity was adjusted to 100 mW cm⁻² (1 sun). The electrolyte was made by saturating $\text{Co}(\text{NO}_3)_2 \cdot 6\text{H}_2\text{O}$ (0.1 M, 99.5%, Wako) in a 1 M potassium phosphate buffer solution. The pH of the buffer was adjusted to 7.0 by adding a potassium hydroxide (KOH; > 85%, Sigma-Aldrich) solution into a phosphoric acid (H_3PO_4 , ≥ 85 wt% in H_2O , Sigma-Aldrich) aqueous solution. Electrodeposition was performed at a constant current density of 50 μA cm⁻² for 5 min under simulated solar light (AM 1.5G). CoO_x deposited or not deposited particle-transferred working electrodes with an area of approximately 0.2–0.3 cm² were positioned in a glass cell. The electrolyte was a 1 M potassium borate buffer (pH 9.0) aqueous solution. The pH was adjusted to 9.0 by adding a KOH (≥ 85%, Sigma-Aldrich) solution into a boric acid (H_3BO_3 , ≥ 99.5 wt% in H_2O , Sigma-Aldrich) aqueous solution. For LSV measurements, 0.1 M of Na_2SO_3 was added as a hole scavenger. PEC measurements



employed a Xe-lamp (MAX-303 Xenon Light Source, 300 W, Asahi Spectra), with a UV-Vis miler module and a cut-off filter (HOYA L42) as the light source ($420 < \lambda < 650$ nm).

Temperature-programmed reduction

TPR equipment consisted of mass flow controllers (KOFLOC, model 3660) and a U-shaped quartz reactor inside an oven. Samples were treated in flowing Ar (20 mL min^{-1}) by increasing their temperature to $400\text{ }^\circ\text{C}$ at $40\text{ }^\circ\text{C min}^{-1}$ and holding for 1 h. After cooling to room temperature, the Ar stream was replaced with the reducing gas, 4% H₂ in Ar (20 mL min^{-1}). The temperature was increased with a heating rate of $10\text{ }^\circ\text{C min}^{-1}$ from room temperature to $850\text{ }^\circ\text{C}$, and the H₂ concentration was monitored using a GC (GC-8A, TCD, Shimadzu) connected to the outlet of the reactor.

Results and discussion

Synthesis and structural characterization of β - and δ -Bi₂O₃ and Bi₃TaO₇

The formation process of the β -Bi₂O₃:Ta (5%) and the δ -Bi₂O₃:Ta (10%) in the solid-state reaction was studied by DTA and *in situ* high temperature XRD measurements. Fig. 1 shows the DTA curves of the pure Bi₂O₃, mixture of Bi₂O₃ and Ta₂O₅ at ratios of Ta/Bi of 0.05 and 0.10. Fig. 2 shows the *in situ* high temperature XRD patterns for the samples at Ta/Bi = 0 (Fig. 2a and b) and 0.050 (Fig. 2c and d). Upon heating the samples, all of the samples show endothermic peaks at $735\text{ }^\circ\text{C}$ (Fig. 1). Accordingly, the new peak assignable to δ -Bi₂O₃ appeared (Fig. 2a), clearly indicating the α to δ transition at this temperature. Pure Bi₂O₃ shows an additional endothermic peak at $830\text{ }^\circ\text{C}$, which can be attributed to the melting of δ -Bi₂O₃.²⁸ Lack of melting behavior with Ta addition suggests that the melting point of Bi₂O₃ is higher than $850\text{ }^\circ\text{C}$. Subsequent decreases in the temperature provided substantial differences in phase transition by varied Ta addition. For pure Bi₂O₃ (Ta/Bi = 0), in Fig. 1, the DTA curve in the cooling process shows two exothermic peaks of curding at $830\text{ }^\circ\text{C}$ and at $620\text{ }^\circ\text{C}$. As the peak at $830\text{ }^\circ\text{C}$ is likely ascribed to solidification, consistent with the literature,²⁸ *in situ* XRD measurements clearly identified that a δ -to- α transition occurred (Fig. 2b), indicating that the original state was recovered during the heating–cooling cycle. For the sample with Ta/Bi = 0.050, an exothermic peak at $580\text{ }^\circ\text{C}$ (Fig. 1) corresponds to the δ -to- β transition (Fig. 2d), the phase that was not obtained without Ta addition. For the sample with Ta/Bi = 0.100, the DTA curve (Fig. 1) did not show any pronounced peaks while cooling. This indicates that the δ phase of the Ta-supplemented Bi₂O₃ was maintained during the cooling process.

Fig. 3a shows the XRD patterns of the samples with a much wider range of Ta/Bi ratios after cooling from the heat treatment at $850\text{ }^\circ\text{C}$ for 5 h. Fig. 3b shows the schematics of the corresponding various crystal structures. The XRD patterns of α -, β -, δ -Bi₂O₃ and Bi₃TaO₇ from the inorganic crystal structure database (ICSD) are shown in Fig. S1 (ESI[†]) as references. While no Ta₂O₅ addition led to the formation of the monoclinic

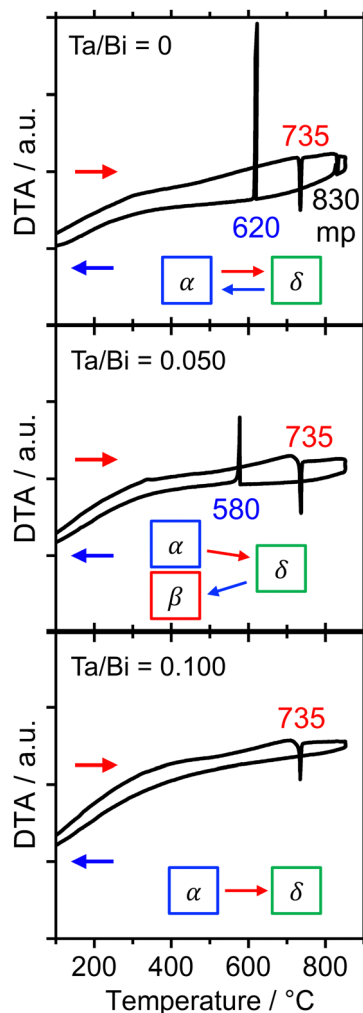


Fig. 1 DTA curves of the Bi₂O₃ samples with Ta/Bi ratios of 0, 0.050, and 0.100. The temperature was increased and subsequently decreased at the rate of $10\text{ }^\circ\text{C min}^{-1}$ in flowing air.

α -Bi₂O₃ structure, a small addition of Ta (Ta/Bi ratio from 0.020 to 0.050) led to the formation of the β -Bi₂O₃ (tetragonal) structure. Further addition of Ta, to give rise to Ta/Bi ratio of 0.100, led to the formation of the δ phase of Bi₂O₃ (cubic, Pn $\bar{3}$ m). The samples with Ta/Bi = 0.167 and 0.333 were identified as the Bi₃TaO₇ phase (cubic, F $\bar{3}$ m). The principal XRD peaks of the obtained β -Bi₂O₃, δ -Bi₂O₃, and Bi₃TaO₇ phases are highlighted in Fig. S2 (ESI[†]). It is of great significance to note that the amount of Ta from 2–5% did not influence the peak position of β -Bi₂O₃, suggesting that the Bi and Ta atoms do not replace each other in the crystal structures of our Ta-supplemented β -Bi₂O₃ samples in a way that affects the lattice constant. On the other hand, for Bi_{3-x}Ta_xO_{3+y} ($x = 1.29$) and Bi₃TaO₇ with the Ta/Bi ratios of 0.167 and 0.333 (Fig. S2b, ESI[†]), the main XRD peaks for the (111) plane can be explained by the replacement of a Ta⁵⁺ cation with a Bi³⁺ cation, which is accompanied by the creation of oxygen vacancies for the charge compensation, and the overall charge electroneutrality of the system is preserved through a mechanism: Bi³⁺ + mpe⁵⁺ + O²⁻.⁶ Finally, the studied samples are compiled in Table 1.



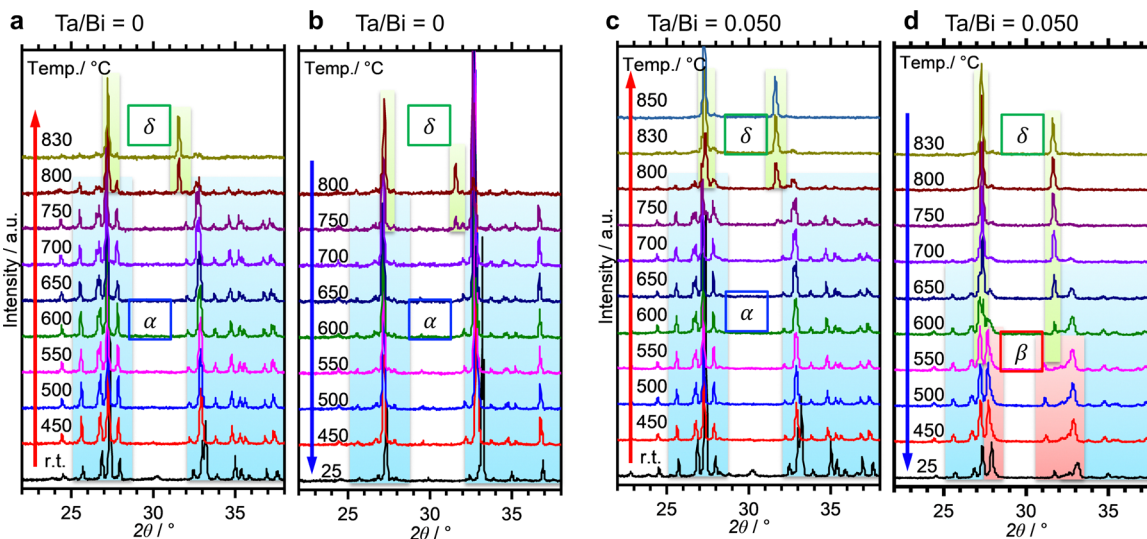


Fig. 2 *In situ* high-temperature XRD for the Bi_2O_3 with Ta/Bi ratios of 0 (a and b) and 0.050 (c and d). The temperature was increased (a and c) and decreased (b and d) at the rate of $10\text{ }^\circ\text{C min}^{-1}$ in static air. The assignments of the XRD peaks are indicated by coloring their backgrounds (blue: α phase; red: β phase; green: δ or cubic phase).

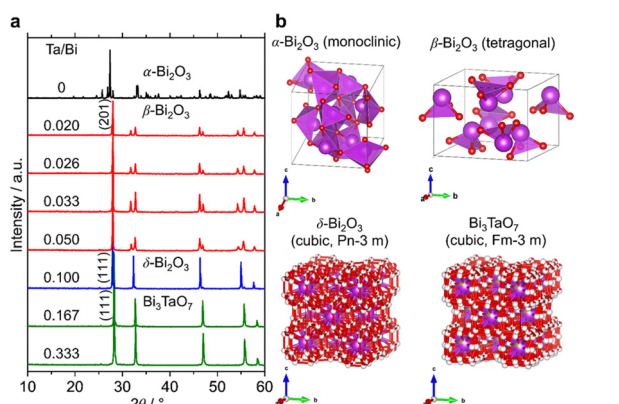


Fig. 3 (a) XRD patterns of the samples at the Ta/Bi ratio. B) Schematics of the crystal structures from ICSD 94229 ($\alpha\text{-Bi}_2\text{O}_3$), 417638 ($\beta\text{-Bi}_2\text{O}_3$), 38436 ($\delta\text{-Bi}_2\text{O}_3$), and 161407 (Bi_3TaO_7).

Fig. S3 (ESI†) shows the SEM images and EDS mappings of the representative samples. Aggregated coarse particles with sizes on the order of micrometers somewhat thermally fused were observed in all samples. From EDX mapping, it can be

Table 1 Ta/Bi ratios in the prepared material, identification of the crystal phase, and the notation in this study

Ta/Bi ratio	Crystal phase	Notation
0	$\alpha\text{-Bi}_2\text{O}_3$ (monoclinic)	$\alpha\text{-Bi}_2\text{O}_3$ (precursor)
0.020	$\beta\text{-Bi}_2\text{O}_3$ (tetragonal)	$\beta\text{-Bi}_2\text{O}_3\text{:Ta}$ (2%)
0.026	$\beta\text{-Bi}_2\text{O}_3$ (tetragonal)	$\beta\text{-Bi}_2\text{O}_3\text{:Ta}$ (2.6%)
0.033	$\beta\text{-Bi}_2\text{O}_3$ (tetragonal)	$\beta\text{-Bi}_2\text{O}_3\text{:Ta}$ (3.3%)
0.050	$\beta\text{-Bi}_2\text{O}_3$ (tetragonal)	$\beta\text{-Bi}_2\text{O}_3\text{:Ta}$ (5%)
0.100	$\delta\text{-Bi}_2\text{O}_3$ (cubic, $Pn\bar{3}m$)	$\delta\text{-Bi}_2\text{O}_3\text{:Ta}$ (10%)
0.167	Bi_3TaO_7 (cubic, $Fm\bar{3}m$)	$\text{Bi}_{3+x}\text{Ta}_{1-x}\text{O}_{7-y}$ ($x = 0.43$)
0.333	Bi_3TaO_7 (cubic, $Fm\bar{3}m$)	Bi_3TaO_7
—	Ta_2O_5 (orthorhombic)	Ta_2O_5 (precursor)

observed that Bi, Ta, and O are well distributed throughout the particles for all samples, indicating the formation of a homogeneous solid solution or Ta-doped Bi_2O_3 .

A small amount of added Ta was observed to play a significant role in structural determination. To identify at which positions the Ta atoms are located in the crystal structures, the local environments of Bi and Ta atoms were studied with XAS measurements, including XANES and EXAFS. All spectra and their analyses are summarized in Fig. S4 (ESI†). The Bi L_3 -edge XANES spectra of $\alpha\text{-Bi}_2\text{O}_3$ (reference), $\beta\text{-Bi}_2\text{O}_3\text{:Ta}$ (5%), $\delta\text{-Bi}_2\text{O}_3\text{:Ta}$ (10%), and Bi_3TaO_7 are shown in Fig. 4a. The spectral shape of the samples basically consists of a main absorption peak (A) located at 13.445 eV , a slight shoulder-like structure just below the main peak (A1, $h\nu \sim 13.42\text{ keV}$), and a single oscillation after the main peak (B, $h\nu \sim 13.46\text{ keV}$). The spectra of $\beta\text{-Bi}_2\text{O}_3\text{:Ta}$ (5.0%), $\delta\text{-Bi}_2\text{O}_3\text{:Ta}$ (10.0%), and Bi_3TaO_7 show a hump (B, $h\nu \sim 13.46\text{ keV}$) followed by a negative feature at higher energies (C, $h\nu \sim 13.47\text{ keV}$), and the spectrum of $\alpha\text{-Bi}_2\text{O}_3$ presents a wide plateau in the energy region immediately after the main peak (B–C, $h\nu \sim 13.46\text{--}13.47\text{ keV}$). This directly indicates that the local environments of Bi in the samples under study are different from those of $\alpha\text{-Bi}_2\text{O}_3$. Moreover, the shift in the shoulder-like structure (A1, $h\nu \sim 13.42\text{ keV}$) at the edge (A, $h\nu \sim 13.445\text{ keV}$) and just below the edge (B, $h\nu \sim 13.46\text{ keV}$) cannot be explained with the linear combination of each other. In other words, the XANES profiles of the samples cannot be explained with the presence of mixed polymorphs.

Next, the Ta L_3 -edge XANES spectra of $\alpha\text{-Bi}_2\text{O}_3$ (reference), $\beta\text{-Bi}_2\text{O}_3\text{:Ta}$ (5%), $\delta\text{-Bi}_2\text{O}_3\text{:Ta}$ (10%), and Bi_3TaO_7 are shown in Fig. 4b. All of the compounds show a main peak (A) at $\sim 9.884\text{ keV}$, but our samples have a double peak corresponding to the split of 5d orbitals, whereas the Ta_2O_5 reference shows only a single peak. This difference is more apparent in the energy region immediately after the main peak because our samples show a hump (B, $h\nu \sim 9.906\text{ keV}$), whereas the Ta_2O_5 reference only shows a shoulder-like

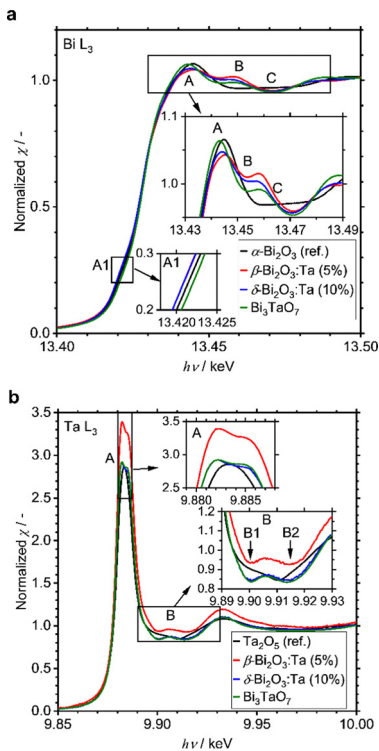


Fig. 4 (a) Comparison of the experimental Bi L₃-edge of α -Bi₂O₃ (reference), β -Bi₂O₃:Ta (5%), δ -Bi₂O₃:Ta (10%), and Bi₃TaO₇. (b) Ta L₃-edge XANES spectra of Ta₂O₅ (reference), β -Bi₂O₃:Ta (5%), δ -Bi₂O₃:Ta (10%), and Bi₃TaO₇.

structure (B1, $h\nu \sim 9.903$ keV) followed by a negative feature at a higher energy (B2, $h\nu \sim 9.910$ keV). These comparisons to the Ta₂O₅ reference show that the local environments around Ta in our studied samples are different from those in the Ta₂O₅ reference.

Similar results are reported in the W L₃-edge XANES spectra of Bi₂WO₆ (octahedral) and Bi₁₄WO₂₄ (tetrahedral) by Wind and coworkers²⁹ and the W L₃-edge XANES spectra of other W-related oxides by Yamazoe and coworkers.⁴⁴ It is reasonable to consider that the differences of the local environments around Ta in the Ta₂O₅ (reference) and our Bi-Ta oxides result from a distortion or oxygen vacancies in the crystal structure induced by Ta addition.

The characteristics of the structural orders around Bi and Ta in the samples are also inferred from the comparison of the Fourier transforms of the EXAFS signals. In Fig. 5, Bi L₃ and Ta L₃ signals of Bi and Ta in the α -Bi₂O₃ reference, α -Bi₂O₃ precursor, and β -Bi₂O₃:Ta (5%) are compared. The main peak at ~ 1.7 Å and double peaks at ~ 3 Å shown in Fig. 5b correspond to the first coordination shell made of oxygen atoms and Bi neighbors.⁴⁵ Additionally, these peaks could be explained by the theoretical radial distribution function calculated from the optimized crystal structures. Fig. 5c shows the Ta L₃-edge EXAFS spectra of the Ta₂O₅ reference, Ta₂O₅ precursor, and β -Bi₂O₃:Ta (5%). The difference between the environments of Ta atoms in the Ta₂O₅ and our β -Bi₂O₃:Ta (5%) is suggested by the Fourier transforms shown in Fig. 5d. The enhancement of the main peak (~ 1.5 Å) can be related to the distortions in distances and angles between the Ta–O bonds in the TaO₆ octahedra.⁴⁶ Furthermore, this distortion is also suggested by the shift of the main peak (~ 1.5 Å) and appearance of the second peak at ~ 2 Å.

The structural orders in the δ -Bi₂O₃:Ta (10%) and Bi₃TaO₇ and their crystal systems were also studied using both Bi L₃ and Ta L₃ edge EXAFS spectra. The EXAFS spectra are shown in Fig. 5a and c and their Fourier transforms are shown in Fig. 5b and d. To perform the theoretical simulation, we assumed that when a Ta atom substitutes Bi sites in the cubic lattice in such a

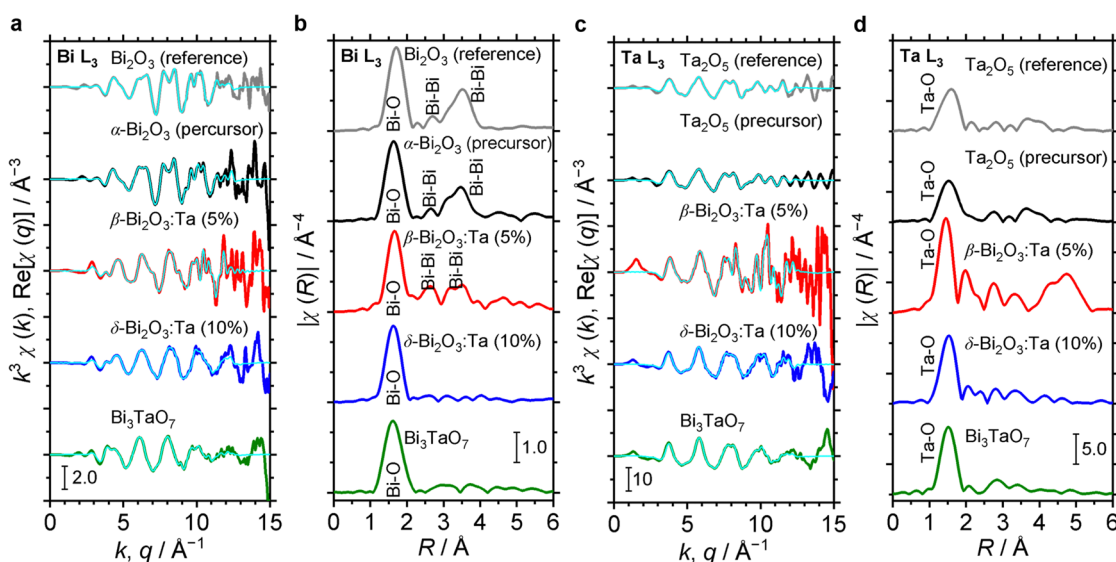


Fig. 5 (a) Comparison of Bi L₃ EXAFS spectra of α -Bi₂O₃ (reference), α -Bi₂O₃ (precursor), β -Bi₂O₃:Ta (5%), δ -Bi₂O₃:Ta (10%) and Bi₃TaO₇. (b) Corresponding Fourier transforms. (c) Comparison of Ta L₃ EXAFS spectra of Ta₂O₅ (reference), Ta₂O₅ (precursor), β -Bi₂O₃:Ta (5%), δ -Bi₂O₃:Ta (10%) and Bi₃TaO₇. (d) Their corresponding Fourier transforms.



way, that the Bi–O distance decreases, the O atoms move close to Bi. This substitutability of Bi and Ta leads to tunability of the bandgap of these cubic-phase B–Ta oxides, as is discussed later. One might initially contend that Ta^{5+} and Bi^{3+} cannot substitute each other in the crystal lattice because the charge in the oxide cannot be balanced. However, the charge has been reasonably explained to be balanced by the change in the occupancy of O sites in previous studies.⁵ Therefore, it can be concluded that by mixing Bi_2O_3 and Ta_2O_5 at a molar ratio of $Ta/Bi = 0.1, 0.33$, the resulting Bi–Ta oxides stabilized and formed a substitutional solid solution with the cubic crystal phase.

Electronic structures and optical properties

The densities of states (DOS) and the charge density maps of β - Bi_2O_3 (201) and δ - Bi_2O_3 (111) slabs were computed using the HSE06 (Heyd–Scuseria–Ernzerhof) exchange–correlation functional, and they are shown in Fig. 6a. The VBM is dominated by O 2p states, whereas the CBM is mostly composed of O 3s and Bi 6p for β - Bi_2O_3 and Bi 6p for δ - Bi_2O_3 . It is worth mentioning that the narrower bandgaps of β - Bi_2O_3 and δ - Bi_2O_3 were explained only by Bi and O, without contribution from the partial density of states of Ta. To study the qualitative nature of chemical bonding in the (201) slab of β - Bi_2O_3 and the (111) slab of δ - Bi_2O_3 , the electron density distribution is presented in

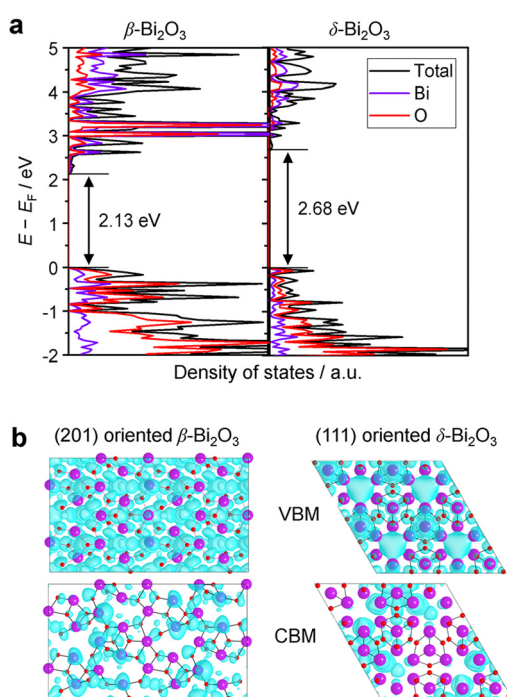


Fig. 6 (a) The total and partial electronic density of states (DOS) of a (201) slab of β - Bi_2O_3 and a (111) slab of δ - Bi_2O_3 . The geometry optimization and electronic structure calculations were performed employing the HSE06 (Heyd–Scuseria–Ernzerhof) exchange–correlation functional along with spin–orbit coupling (SOC) corrections, as implemented in VASP (Vienna *Ab initio* Simulation Package). (b) Charge density maps obtained for the VBM and CBM electronic states of the (201) β - Bi_2O_3 and (111) δ - Bi_2O_3 slabs. The isosurface value is set at 6.7×10^{-3} au.

Fig. 6b. Comparing these two model surfaces, we observe more depletion of charge on Bi in (111) δ - Bi_2O_3 and more σ character of bonds on the surface of δ - Bi_2O_3 , while β - Bi_2O_3 exhibits mixed bonds. However, there is a lack of strong hybridization (observed also in DOS in Fig. 6a) between Bi and O states in both surfaces; thus, fewer covalent bonds between atoms will exist, which could suppress the charge carrier transport. Moreover, we computed the effective mass tensors of the photogenerated holes (m_h^*) and electrons (m_e^*) at the band edges of the (201) slab of β - Bi_2O_3 and the (111) slab of δ - Bi_2O_3 using their electronic band structure, which were obtained from the PBE exchange–correlation functional; these results are listed in Table 2. The values are substantially larger than the benchmarking 0.5 m_0 for good charge carrier transport,^{47–49} even compared to those based on the Bi–Ti–O system reported in our previous studies.^{50,51} Large values of both electron mass and hole effective mass for both the (201) slab of β - Bi_2O_3 and (111) slab of δ - Bi_2O_3 predict poor charge separation capability of the materials and the resultant poor photocatalytic properties. The optimized structures and the local potential in the z -direction are shown in Fig. S5 (ESI†).

To determine the absorption characteristics of Bi-based samples, DR-UV-vis spectroscopy was used and compared with the simulated absorption coefficient as a function of wavelength. The results are shown in Fig. 7. The Kubelka–Munk functions of the representative ones (Fig. 7a) show that for the pure α - Bi_2O_3 precursor, the adsorption edge was 445 nm in the near UV region, whereas that of β - Bi_2O_3 :Ta (5%) was 550 nm. The absorption edges of the δ - Bi_2O_3 :Ta (10%) and Bi_3TaO_7 were 530 and 440 nm, respectively. The bandgap energy calculation yields values of 2.8, 2.2, 2.3, and 2.8 eV for α - Bi_2O_3 , β - Bi_2O_3 :Ta (5%), δ - Bi_2O_3 :Ta (10%), and Bi_3TaO_7 , respectively. The visible-light responsiveness of β - Bi_2O_3 and δ - Bi_2O_3 were simulated on our slab models whose structures were optimized without adding Ta. The simulated absorption spectra are shown in Fig. 7b, and their absorption edges nearly correspond to those of the experimental spectra. In general, the degree of absorption coefficient is considered low for these Bi_2O_3 , compared to other general compound-based semiconductors.⁴⁷

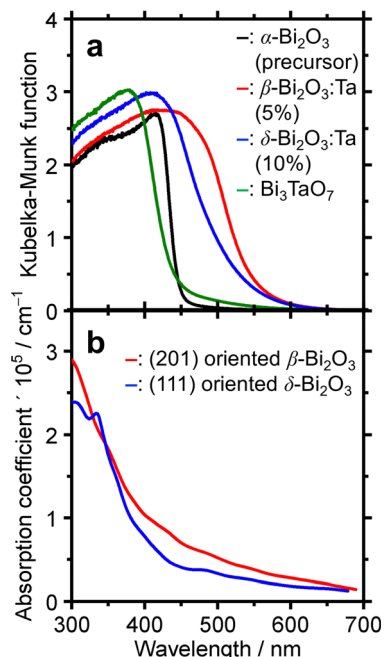
Because it remained possible that the visible-light responsiveness (2.2 eV bandgap) is derived from the existence of defects especially caused by added Ta in the β - Bi_2O_3 :Ta (5%), photoluminescence spectroscopy was conducted. The results are shown in Fig. S6 (ESI†). For the α - Bi_2O_3 (precursor) shown in Fig. S6a (ESI†), the emission spectra triggered by 400 nm excitation light show a peak at 500–700 nm attributable to the existence of a defect level within the bandgap. However, the photoluminescence spectrum of our β - Bi_2O_3 :Ta (5%) shown in Fig. S6b (ESI†) did not exhibit noticeable peaks other than a small peak at 560 nm attributed to near bandgap emission. This result does not contradict the statement that the photon absorption at band edges is mainly β - Bi_2O_3 bandgap excitation.

The band alignment of the CBM and the VBM positions of the synthesized samples was experimentally estimated by using PESA. The VBM potentials estimated by ionization potentials were obtained by the crossing point of the linear part of the

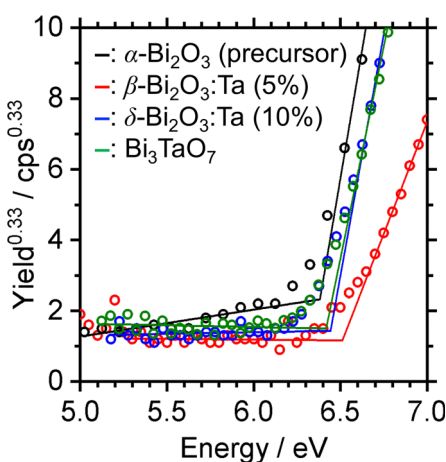


Table 2 Summary of electronic, dielectric, and optical properties of (201) oriented β - Bi_2O_3 and (111) oriented δ - Bi_2O_3 slabs

	(201) oriented β - Bi_2O_3	(111) oriented δ - Bi_2O_3
Electronic dielectric constant ϵ_{∞} along: xx (yy)	6.0 (4.8)	5.0 (7.3)
Macroscopic dielectric constant ϵ_r along: xx (yy)	98 (93)	100 (119)
Effective electron mass m_e^*/m_e	1.2	3.2
Effective hole mass m_h^*/m_e	20	13
VBM (vs. vacuum in eV)	-5.59	-5.36
CBM (vs. vacuum in eV)	-3.46	-2.68
Bandgap (eV)	2.13	2.68

Fig. 7 (a) The DR-UV-vis spectra of α - Bi_2O_3 (precursor), β - Bi_2O_3 :Ta (5%), δ - Bi_2O_3 :Ta (10%), and Bi_3TaO_7 . (b) Simulated UV-visible optical absorption spectra of (201) oriented β - Bi_2O_3 and (111) oriented δ - Bi_2O_3 slabs.

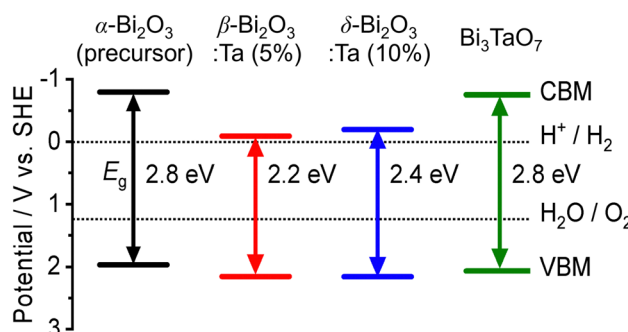
curve with the background from PESA. The spectra of representative samples are shown in Fig. 8, and all other spectra of

Fig. 8 Photoelectron spectra in air (PESA) of α - Bi_2O_3 (precursor), β - Bi_2O_3 :Ta (5%), δ - Bi_2O_3 :Ta (10%), and Bi_3TaO_7 .

the $\text{Bi}-\text{Ta}$ oxides are shown in Fig. S7 (ESI[†]). The VBM do not shift significantly but remain constant at 6.4–6.6 eV vs. vacuum (*i.e.*, 2.0–2.2 eV vs. SHE), as expected from the contribution of O 2p orbitals. The determined band positions are summarized in Fig. 9 together with the Ta/Bi ratio and the resulting crystal phase. The results suggest that the conduction band positions are largely altered while valence band positions are relatively consistent.

To check the photoresponsive behavior of α - Bi_2O_3 (precursor) and β - Bi_2O_3 :Ta (5%), LSV (linear sweep voltammetry) under chopped-light illumination was conducted for CoO_x/α - Bi_2O_3 (precursor)/Ti-Sn, and CoO_x/β - Bi_2O_3 :Ta (5%)/Ti-Sn particle-transferred electrodes. The result is shown in Fig. 10. The CoO_x/α - Bi_2O_3 (precursor)/Ti-Sn electrode did not exhibit a pronounced response to the light, but the CoO_x/β - Bi_2O_3 :Ta (5%)/Ti-Sn electrode showed a pronounced anodic photocurrent. Because the Xe-lamp was used with a cut-off filter as the light source ($420 < \lambda < 650$ nm), this spectrum indicates that this material can utilize visible light to produce photo-excited holes and electrons. The onset potential of the sacrificial reagent oxidation reaction was found to be 0.5 V vs. RHE under light illumination, despite the fact that it was 1.0 V vs. RHE under dark conditions. The anodic photocurrent of 0.1 mA cm^{-2} was found to be 1.25 V vs. RHE.

To determine the dielectric properties of β - Bi_2O_3 :Ta (5%) and δ - Bi_2O_3 :Ta (10%), we computed their dielectric constants and effective masses. In a dielectric material, the static dielectric constant (ϵ_r) has contributions from two factors: the electron density (ϵ_{∞}) and the ion vibrations (ϵ_{vib}). The dielectric constants and effective masses are listed in Table 3, and the real and imaginary parts of the dielectric functions obtained

Fig. 9 The experimental band positions of α - Bi_2O_3 (precursor), β - Bi_2O_3 :Ta (5%), δ - Bi_2O_3 :Ta (10%), and Bi_3TaO_7 . The bandgap (E_g) and valence band maximum (VBM) of each sample were determined by DR-UV-vis spectroscopy (Fig. 7a) and photoelectron spectroscopy in air (PESA) (Fig. 8), respectively.

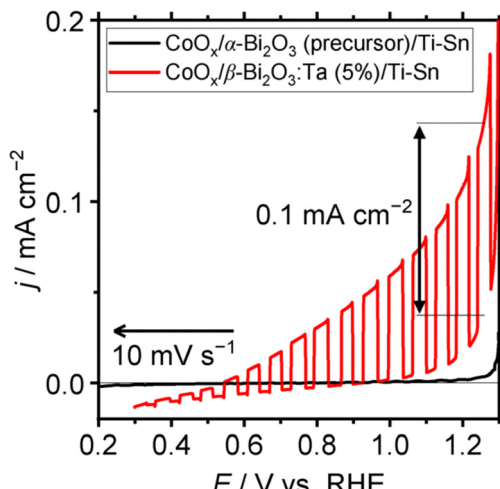


Fig. 10 LSV at 10 mV s^{-1} under light chops for $\text{CoO}_x/\alpha\text{-Bi}_2\text{O}_3$ (precursor)/Ti-Sn and $\text{CoO}_x/\beta\text{-Bi}_2\text{O}_3\text{:Ta}$ (5%)/Ti-Sn in 1 M potassium borate aqueous solution (pH 9). Sacrificial reagent: 0.1 M Na_2SO_3 ; RE: $\text{Hg}/\text{Hg}_2\text{Cl}_2$ /saturated KCl; CE: Pt wire; light source: Xe-lamp (MAX-303, 300 W) with cut-off filter (L42), $>420 \text{ nm}$; temperature: 25°C .

using HSE06 and SOC are shown in Fig. S8 (ESI†). With these calculations, the charge carriers were found to be heavy, indicating poor photocatalytic properties.

Thermal redox properties

To investigate the difference of reducibility of our Bi-based oxides and consider an application for them as a material that is accompanied by thermal redox, TPR measurements were performed. The TPR profiles of the studied Bi-Ta oxides are shown in Fig. 11. A broad reduction peak of $\alpha\text{-Bi}_2\text{O}_3$ (precursor) appeared at 700°C . The atomic ratio of consumed H_2 to Bi contained in the sample (H_2/Bi ratio, Fig. 11) was calculated to be 1.58, and the total hydrogen consumption accounted for the complete reduction of the $\alpha\text{-Bi}_2\text{O}_3$ (precursor) sample. The broadness of the peak can be attributed to the relatively large sizes of the $\alpha\text{-Bi}_2\text{O}_3$ (precursor) particles, as seen in the SEM images (Fig. S3, ESI†). The peak was tailed to 400°C , suggesting a faster reduction of the surface. TPR was also performed on the Ta_2O_5 (precursor), but substantial reduction was not observed throughout this temperature range up to 900°C . $\beta\text{-Bi}_2\text{O}_3\text{:Ta}$ (5%) showed reduction starting at around 400°C , with a maximum at 640°C , indicating facilitated reduction compared to $\alpha\text{-Bi}_2\text{O}_3$ (precursor). Both the H_2/Bi and H_2/O ratios of 1.56 and 0.96 indicated the complete reduction of Bi atoms. $\delta\text{-Bi}_2\text{O}_3\text{:Ta}$ (10%) had a reduction peak starting at 300°C , a markedly low

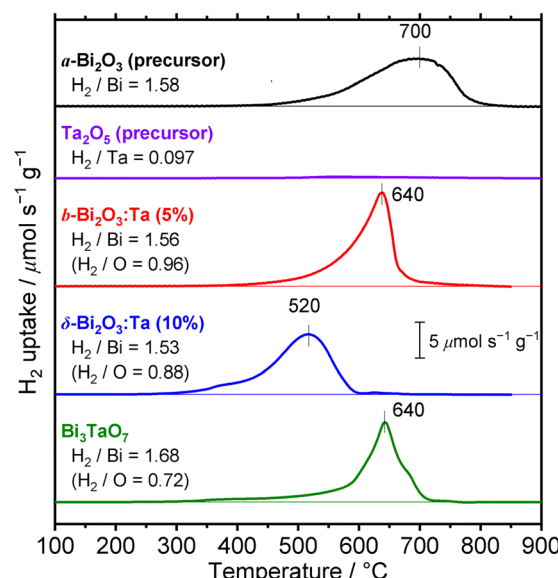
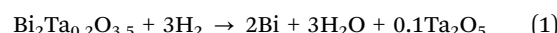
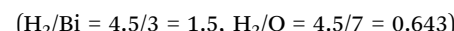
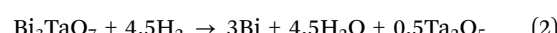


Fig. 11 TPR profiles of $\alpha\text{-Bi}_2\text{O}_3$ (precursor), Ta_2O_5 (precursor), $\beta\text{-Bi}_2\text{O}_3\text{:Ta}$ (5%), $\delta\text{-Bi}_2\text{O}_3\text{:Ta}$ (10%), and Bi_3TaO_7 . The total hydrogen consumptions are expressed in moles of H_2 consumed per mole of metal atoms (H_2/Bi or H_2/Ta) and moles of H_2 consumed per mole of O atoms (H_2/O). The samples were pretreated in Ar (20 mL min^{-1}) at 400°C before each measurement. The measurements were conducted on 20 mg of samples in 4% H_2 (in Ar, 20 mL min^{-1}) with a heating rate of $10^\circ\text{C min}^{-1}$.

temperature, with a maximum at 520°C , again the lowest temperature among the samples investigated. These findings suggest that reduction of both bulk and the surface of $\delta\text{-Bi}_2\text{O}_3\text{:Ta}$ (10%) was easiest among the samples. This facilitated redox property might be explained by the high mobility of oxygen species related to the low occupancy of O sites due to its defective crystal structure. The consumption of hydrogen ($\text{H}_2/\text{Bi} = 1.53$ and $\text{H}_2/\text{O} = 0.88$) can be explained if it is assumed that the Ta atoms are not reduced, and that only Bi atoms are reduced, as expressed by the following reaction (note that $\delta\text{-Bi}_2\text{O}_3\text{:Ta}$ [10%] is expressed as $\text{Bi}_2\text{Ta}_{0.2}\text{O}_{3.5}$):



Bi_3TaO_7 showed a reduction peak at 640°C , which appeared at a higher temperatures than that of $\delta\text{-Bi}_2\text{O}_3\text{:Ta}$ (10%); this may be because $\delta\text{-Bi}_2\text{O}_3\text{:Ta}$ (10%) has a less defective structure than Bi_3TaO_7 . The peak was tailed to 300°C , but the tailing was not as pronounced as that of $\delta\text{-Bi}_2\text{O}_3\text{:Ta}$ (10%). The stoichiometry of the consumption of hydrogen ($\text{H}_2/\text{Bi} = 1.68$ and $\text{H}_2/\text{O} = 0.72$) can be roughly explained by the following reaction:



Among these oxides, $\delta\text{-Bi}_2\text{O}_3\text{:Ta}$ (10%) appeared to have a TPR peak at the lowest temperature, meaning the highest thermal

Table 3 Summary of the computed properties for $\beta\text{-Bi}_2\text{O}_3$ and $\delta\text{-Bi}_2\text{O}_3$

	(201) $\beta\text{-Bi}_2\text{O}_3$	(111) $\delta\text{-Bi}_2\text{O}_3$
ε_∞ along x	6.0	5.0
ε_∞ along y	4.8	7.3
ε_{vib} along x	98	100
ε_{vib} along y	93	119
m_e^*/m_e	1.2	3.2
m_h^*/m_e	19.9	12.5



redox properties. This material is expected to be utilized as a catalyst or its support for reactions that are accompanied by oxidation or reduction. Further investigations into the applications of this material as a thermal catalyst or its support are expected.

Conclusions

In summary, this investigation of the Ta-supplemented bismuth oxides, such as α -Bi₂O₃, β -Bi₂O₃, δ -Bi₂O₃ and Bi₃TaO₇, confirms that the crystal structures and optoelectronic properties of these oxides are altered according to the amount of added Ta (as Ta₂O₅). Heat treatment at 850 °C and cooling of Bi₂O₃ with different amounts of added Ta controllably led to the formation of α -Bi₂O₃, β -Bi₂O₃, and δ -Bi₂O₃. Among them, β -Bi₂O₃ was found to be a promising visible-light harvesting material, as it has the narrowest bandgap of 2.2 eV. DFT calculations using the HSE exchange–correlation functional and PESA measurements demonstrate that the conduction band has a large contribution from Bi orbitals in β -Bi₂O₃ and δ -Bi₂O₃. We confirmed that the presence of added Ta is not essential to alter the band structures of bismuth oxides by causing a defect level but, rather, by changing the crystal phase of bismuth oxides. However, the DFT calculations also suggested that β -Bi₂O₃ and δ -Bi₂O₃, which have bandgaps narrow enough to absorb visible light, are limited in their applicability as a photocatalyst due to their large effective masses and resultant low charge mobilities. In addition, different Bi₂O₃ polymorphs exhibited distinctive reducibility upon hydrogen treatment at high temperatures, showing that δ -Bi₂O₃ was reduced at the lowest temperature among the samples investigated. The wide range of methodologies adopted in this study and the knowledge gained into the semiconductor structure of a mixed oxide through these methodologies will allow us to identify and understand other novel candidate materials for applications such as photocatalysis and thermal catalysis.

Author contributions

All authors contributed to writing the manuscript. All authors approved the final version of the manuscript.

Conflicts of interest

There are no conflicts to declare.

Acknowledgements

This work was supported by the Mohammed bin Salman Center for Future Science and Technology for Saudi-Japan Vision 2030 at the University of Tokyo (MbSC2030). LC and RA acknowledge Shaheen and HPC Core Labs team at KAUST.

Notes and references

- 1 J. S. Ahn, M. A. Camaratta, D. Pergolesi, K. T. Lee, H. Yoon, B. W. Lee, D. W. Jung, E. Traversa and E. D. Wachsman, *J. Electrochem. Soc.*, 2010, **157**, B376.
- 2 R. D. Bayliss, S. N. Cook, S. Kotsantonis, R. J. Chater and J. A. Kilner, *Adv. Energy Mater.*, 2014, **4**, 1301575.
- 3 X. Kuang, J. L. Payne, M. R. Johnson and I. Radosavljevic Evans, *Angew. Chem., Int. Ed.*, 2012, **51**, 690–694.
- 4 R. Punn, A. M. Feteira, D. C. Sinclair and C. Greaves, *J. Am. Chem. Soc.*, 2006, **128**, 15386–15387.
- 5 K. Firman, K. B. Tan, C. C. Khaw, Z. Zainal, Y. P. Tan and S. K. Chen, *J. Mater. Sci.*, 2017, **52**, 10106–10118.
- 6 M. Gambino, F. Giannici, A. Longo, S. Di Tommaso, F. Labat and A. Martorana, *J. Phys. Chem. C*, 2015, **119**, 26367–26373.
- 7 R. Oka, Y. Shobu and T. Masui, *ACS Omega*, 2019, **4**, 7581–7585.
- 8 M. Li, F. Li and P. G. Yin, *Chem. Phys. Lett.*, 2014, **601**, 92–97.
- 9 S. J. A. Moniz, D. Bhachu, C. S. Blackman, A. J. Cross, S. Elouali, D. Pugh, R. Q. Cabrera and S. Vallejos, *Inorg. Chim. Acta*, 2012, **380**, 328–335.
- 10 M. Schlesinger, S. Schulze, M. Hietschold and M. Mehring, *Dalton Trans.*, 2013, **42**, 1047–1056.
- 11 Y. Lu, Y. Zhao, J. Zhao, Y. Song, Z. Huang, F. Gao, N. Li and Y. Li, *Cryst. Growth Des.*, 2015, **15**, 1031–1042.
- 12 L. Zhang, Y. Shi, Z. Wang, C. Hu, B. Shi and X. Cao, *Appl. Catal., B*, 2020, **265**, 118563.
- 13 S. Singh and R. Sharma, *Sol. Energy Mater. Sol. Cells*, 2018, **186**, 208–216.
- 14 Y. C. Wu, Y. C. Chaing, C. Y. Huang, S. F. Wang and H. Y. Yang, *Dyes Pigm.*, 2013, **98**, 25–30.
- 15 S. Zhong, S. Zou, X. Peng, J. Ma and F. Zhang, *J. Sol-Gel Sci. Technol.*, 2015, **74**, 220–226.
- 16 H. Sudrajat, *J. Nanopart. Res.*, 2017, **19**, 1–8.
- 17 J. C. Medina, M. Bizarro, P. Silva-Bermudez, M. Giorcelli, A. Tagliaferro and S. E. Rodil, *Thin Solid Films*, 2016, **612**, 72–81.
- 18 H. Sudrajat and P. Sujardworakun, *Mater. Des.*, 2017, **130**, 501–511.
- 19 S. Zhu, L. Lu, Z. Zhao, T. Wang, X. Liu, H. Zhang, F. Dong and Y. Zhang, *J. Phys. Chem. C*, 2017, **121**, 9394–9401.
- 20 H. Sudrajat and S. Hartuti, *Adv. Powder Technol.*, 2019, **30**, 983–991.
- 21 S. J. A. Moniz, C. S. Blackman, C. J. Carmalt and G. Hyett, *J. Mater. Chem.*, 2010, **20**, 7881–7886.
- 22 G. D. Lim, J. H. Yoo, M. Ji and Y. I. Lee, *J. Alloys Compd.*, 2019, **806**, 1060–1067.
- 23 C. Chang, H.-C. Yang, N. Gao and S.-Y. Lu, *J. Alloys Compd.*, 2018, **738**, 138–144.
- 24 N. R. Khalid, Z. Israr, M. B. Tahir and T. Iqbal, *Int. J. Hydrogen Energy*, 2020, **45**, 8479–8489.
- 25 Y. Shi, L. Luo, Y. Zhang, Y. Chen, S. Wang, L. Li, Y. Long and F. Jiang, *Ceram. Int.*, 2017, **43**, 7627–7635.
- 26 H. Sudrajat, *Superlattices Microstruct.*, 2017, **109**, 229–239.
- 27 A. H. Zahid and Q. Han, *Nanoscale*, 2021, **13**, 17687–17724.
- 28 G. Guenther and O. Guillon, *J. Mater. Res.*, 2014, **29**, 1383–1392.
- 29 J. Wind, J. Polt, Z. Zhang, D. A. Blom, T. Vogt, R. L. Withers and C. D. Ling, *Chem. Mater.*, 2017, **29**, 9171–9181.



30 V. Fruth, A. Ianculescu, D. Berger, S. Preda, G. Voicu, E. Tenea and M. Popa, *J. Eur. Ceram. Soc.*, 2006, **26**, 3011–3016.

31 H. N. Lin, M. S. Chen, Y. H. Chang, P. Y. Lee and C. K. Lin, *Materials*, 2019, **12**(12), 1947.

32 J. L. Ortiz-Quinonez, I. Zumeta-Dubé, D. Díaz, N. Navá-Etzana, E. Cruz-Zaragoza and P. Santiago-Jacinto, *Inorg. Chem.*, 2017, **56**, 3394–3403.

33 J. A. H. Dreyer, S. Pokhrel, J. Birkenstock, M. G. Hevia, M. Schowalter, A. Rosenauer, A. Urakawa, W. Y. Teoh and L. Mädler, *CrystEngComm*, 2016, **18**, 2046–2056.

34 W. Humphrey, A. Dalke and K. Schulten, *J. Mol. Graphics*, 1996, **14**, 33–38.

35 W. M. H. Sachtler, G. J. H. Dorgelo and A. A. Holscher, *Surf. Sci.*, 1966, **5**, 221–229.

36 G. Kresse and J. Hafner, *Phys. Rev. B: Condens. Matter Mater. Phys.*, 1993, **48**, 13115–13118.

37 G. Kresse and J. Furthmüller, *Phys. Rev. B: Condens. Matter Mater. Phys.*, 1996, **54**, 11169–11186.

38 P. E. Blöchl, *Phys. Rev. B: Condens. Matter Mater. Phys.*, 1994, **50**, 17953–17979.

39 H. J. Monkhorst and J. D. Pack, *Phys. Rev. B: Solid State*, 1976, **13**, 5188–5192.

40 J. P. Perdew and Y. Wang, *Phys. Rev. B: Condens. Matter Mater. Phys.*, 1992, **45**, 13244–13249.

41 J. Heyd and G. E. Scuseria, *J. Chem. Phys.*, 2004, **121**, 1187–1192.

42 J. E. Peralta, J. Heyd, G. E. Scuseria and R. L. Martin, *Phys. Rev. B: Condens. Matter Mater. Phys.*, 2006, **74**, 073101.

43 M. Gmitra, S. Konschuh, C. Ertler, C. Ambrosch-Draxl and J. Fabian, *Phys. Rev. B: Condens. Matter Mater. Phys.*, 2009, **80**, 235431.

44 S. Yamazoe, Y. Hitomi, T. Shishido and T. Tanaka, *J. Phys. Chem. C*, 2008, **112**, 6869–6879.

45 M. A. Laguna-Marco, C. Piquer, A. G. Roca, R. Boada, M. Andrés-Vergés, S. Veintemillas-Verdaguer, C. J. Serna, A. Iadecola and J. Chaboy, *Phys. Chem. Chem. Phys.*, 2014, **16**, 18301–18310.

46 J. Ribeiro, G. Tremiliosi-Filho, P. Olivi and A. R. Andrade, *Mater. Chem. Phys.*, 2011, **125**, 449–460.

47 O. Madelung, *Semiconductors: Data Handbook*, Springer, Berlin Heidelberg, 2012.

48 S. Adachi, *GaAs and Related Materials: Bulk Semiconducting and Super-lattice Properties*, World Scientific, 1994.

49 T. Le Bahers, M. Rérat and P. Sautet, *J. Phys. Chem. C*, 2014, **118**, 5997–6008.

50 S. Lardhi, D. Noureldine, M. Harb, A. Ziani, L. Cavallo and K. Takanabe, *J. Chem. Phys.*, 2016, **144**, 134702.

51 D. Noureldine, S. Lardhi, A. Ziani, M. Harb, L. Cavallo and K. Takanabe, *J. Mater. Chem. C*, 2015, **3**, 12032–12039.

